

**Controlled interconversion of quantized spin wave modes via local magnetic fields**Zhizhi Zhang,<sup>1,2</sup> Michael Vogel,<sup>1</sup> José Holanda,<sup>1</sup> Junjia Ding,<sup>1</sup> M. Benjamin Jungfleisch,<sup>3</sup> Yi Li,<sup>1,4</sup> John E. Pearson,<sup>1</sup> Ralu Divan,<sup>5</sup> Wei Zhang,<sup>4</sup> Axel Hoffmann,<sup>1</sup> Yan Nie,<sup>2,\*</sup> and Valentine Novosad<sup>1,†</sup><sup>1</sup>*Materials Science Division, Argonne National Laboratory, Argonne, Illinois 60439, USA*<sup>2</sup>*School of Optical and Electronic Information, Huazhong University of Science and Technology, Wuhan 430074, China*<sup>3</sup>*Department of Physics and Astronomy, University of Delaware, Newark, Delaware 19716, USA*<sup>4</sup>*Department of Physics, Oakland University, Rochester, Michigan 48309, USA*<sup>5</sup>*Center for Nanoscale Materials, Argonne National Laboratory, Argonne, Illinois 60439, USA*

(Received 25 April 2019; published 24 July 2019)

In the emerging field of magnonics, spin waves are considered for information processing and transmission at high frequencies. Accordingly, the manipulation of propagating spin waves in nanostructured waveguides for novel functionality has attracted increased attention. Excitations with uniform magnetic fields in such waveguides favor symmetric spin-wave modes with odd quantization numbers. Interference between multiple odd spin-wave modes leads to a periodic self-focusing effect of the propagating spin waves. In this work we demonstrate how antisymmetric spin-wave modes with even quantization numbers can be induced by local magnetic fields in a well-controlled fashion. The resulting interference patterns are discussed within an analytical model and experimentally demonstrated using microfocused Brillouin light scattering.

DOI: [10.1103/PhysRevB.100.014429](https://doi.org/10.1103/PhysRevB.100.014429)**I. INTRODUCTION**

Collective excitations of the electronic spin structure known as spin waves (SWs) and their quasiparticles, i.e., magnons, are promising for high-frequency information processing and transmission [1–4]. Additional functionality can be gained because spin waves can also be coupled to other wavelike excitations, such as photons [5,6] and phonons [7]. Furthermore, many classical wave phenomena, such as diffraction [8,9], reflection and refraction [10–12], interference [13,14], and the Doppler effect [15,16], were observed with spin waves. At the same time, quantum mechanical interactions, such as the magnon scattering [17–19] and their interactions with other quasiparticles [20] were observed as well, providing additional avenues for utilizing spin waves. Understanding these phenomena is key to realizing practical applications in the rapidly emerging field of magnonics.

Spin waves can encode information either in their amplitude [21,22] or their phase [23,24]. Compared with conventional electronic approaches, spin waves possess several advantages, including potentially reduced heat dissipation [25], wave-based computation [26,27], and strong nonlinearities [28,29], which may all be beneficial for efficient data processing. The recent emerging interest in magnonics can be attributed to the improvement of modern microfabrication, which enables the realization of the magnetic microstrips with characteristic dimensions ranging from several micrometers to below a hundred nanometers [30,31], as well as integrated microantenna for excitations [32,33]. When such a

magnetic microstripe is magnetized with an external magnetic field ( $H_{\text{ext}}$ ) in-plane and perpendicular to the stripe direction, the spin waves are called Damon-Eshbach modes [34] and can be localized either at the edge or in the center region, depending on their frequencies [35,36]. Previous studies have demonstrated that spin waves in the center region (so-called waveguide spin waves) are quantized into several discrete modes because of the confinement along the width of the waveguide [37]. In addition, generally a homogenous radio frequency (*rf*) field can only excite lateral symmetrically distributed, odd waveguide spin-wave modes [38]. The interference of several of these modes results in a periodic self-focusing where the waveguide spin waves propagate in diamond chainlike channels [32,39,40]. Self-channeling and nonlinear beam formation of backward volume magnetostatic waves were also reported for thick yttrium iron garnet (YIG) single crystal films subjected to high-power microwave excitations [41,42]. Their properties can be investigated in more details using optical methods than microwave means [43].

In magnonic applications, the manipulation of the spin-wave propagation is of great significance for the functionality of such devices, especially for logic elements [21–24] and multiplexers [44]. Toward this end, the constructive or destructive interference of multiple coherent spin waves impact the spatial intensity distributions of the resultant waves and therefore controls the energy and information flows associated with the spin waves. Previous studies focused mostly on odd spin-wave modes because they are easier to generate with homogeneous excitations. In this work, we demonstrate the controlled interconversions of odd and even waveguide spin waves in YIG microstrips by breaking the symmetry via well-defined local inhomogeneous magnetic fields. This approach allows for a reconfigurable mechanism of mode conversion, unlike previous experiments where the symmetry

\*nieyan@hust.edu.cn

†novosad@anl.gov

is broken by the geometry of the waveguide or using a tilted excitation antenna [45,46].

In our work, the local magnetic fields are generated from permalloy (Py, Ni<sub>81</sub>Fe<sub>19</sub>) micromagnets placed asymmetrically next to the YIG waveguide. (Note that the saturation magnetization ( $M_s$ ) for Py is about five times larger than that for YIG). In addition, the Py micromagnets can easily perturb the effective magnetic field ( $H_{\text{eff}}$ ) in YIG structures, changing the symmetry of the propagating spin waves in YIG. By using a combination of theoretical calculations, magnetic simulations, and microfocused Brillouin light scattering ( $\mu$ -BLS), we demonstrate that the different spin-wave channels are essentially controlled by the phase difference between odd and even modes, which can be practically modulated through the relative position of the micromagnets and the magnitude of the external magnetic field.

## II. ANALYTICAL CALCULATIONS

We consider a thin YIG microstripe with a thickness of  $t = 50$  nm, width of  $w = 3 \mu\text{m}$ , and infinite length of  $l$  magnetized in-plane in a direction perpendicular to the length through a magnetic field  $H_0 = 650$  Oe, as shown in the inset of Fig. 1(a). The material parameters used in the theoretical calculation are  $M_s(\text{YIG}) = 1960$  G, exchange constant  $A(\text{YIG}) = 4 \times 10^{-7}$  erg/cm, and damping factor  $\alpha(\text{YIG}) = 7.561 \times 10^{-4}$  [31].

For the first step, the waveguide spin-wave modes in a microstripe can be described based on the dipole-exchange theory of the spin-wave dispersion spectra in a continuous magnetic film [47,48]. This theory provides an explicit relationship between the wave vector  $\mathbf{k} = (k_x, k_y)$  and the frequency  $f$  of the spin waves:

$$f = \gamma \sqrt{(H_0 + M_s(1 - p + \lambda_{\text{ex}}^2 k^2)) \times \left( H_0 + M_s \left( p \frac{k_x^2}{k^2} + \lambda_{\text{ex}}^2 k^2 \right) \right)}, \quad (1)$$

where  $p = 1 - (1 - e^{-kt})/kt$ ,  $k^2 = k_x^2 + k_y^2$ , and  $\lambda_{\text{ex}} = (2A/M_s^2)^{1/2}$  is the exchange length [49]. The two limiting relations for  $k_x = 0$  and  $k_y = 0$  correspond to the Damon-Eshbach and backward volume modes. Furthermore, there are scientific constants for the gyromagnetic ratio  $\gamma = 2.8$  MHz/Oe.

Neglecting the effect of the demagnetizing field ( $H_d$ ), which is important only close to the edges of the microstripe, the waveguide spin waves are confined along the width direction and can be described as the quantization of planar spin waves propagating along the length direction. Consequently, only waveguide spin waves with  $k_y$  components satisfying the resonant standing waves conditions can propagate in the microstripe. These  $k_y$  components are a set of discrete values, described by a simple expression:

$$k_{y,n} = n\pi/w. \quad (2)$$

Combining Eqs. (1) and (2), the dispersion relation curves for each mode with  $n = 1, 2, \dots, 5$  are plotted in Fig. 1(a). Only lateral modes with odd quantization numbers  $n$  can be excited under a uniform  $rf$  magnetic field, and their amplitudes decrease with increasing  $n$  as  $1/n$  [38]. With a frequency of  $f = 4$  GHz we can calculate the corresponding  $k_{x,n}$ . Then, the spatial distribution of the  $n$ th mode's dynamic magnetization and their integrated superpositions, i.e., the interference of the odd modes, can be written as

$$m_n(x, y) \propto \frac{1}{n} \sin\left(\frac{n\pi}{w}y\right) \cos(k_{x,n}x - 2\pi ft + \varphi_n) \quad (3)$$

and

$$I_\Sigma(x, y) \propto \left( \sum_n m_n(x, y) \right)^2, \quad (4)$$

where  $\varphi_n$  is the excitation phase. The patterns of the first three odd modes are mapped in Fig. 1(b) for  $-2\pi ft + \varphi_n = 0$ ,

which coincides with the maximum dynamic magnetization at  $x = 0$ . According to Eqs. (3) and (4), the major contribution to  $I_\Sigma(x, y)$  comes from the first few modes because the intensity of the modes is proportional to  $1/n^2$ . Therefore,  $n = 11$  is sufficient for an accurate analysis and the corresponding interference pattern is mapped as shown in the upper panel of Fig. 1(c). To determine the amplitude of the procession of every spin, we calculated the maximum values of  $I_\Sigma(x, y)$  within  $-2\pi ft + \varphi_n \in (0, 2\pi)$ :

$$I(x, y) = \max[I_\Sigma(x, y) : -2\pi ft + \varphi_n \in (0, 2\pi)], \quad (5)$$

where  $I(x, y)$  is the amplitude of the waveguide spin wave in materials (without considering damping effects), which can be detected using the  $\mu$ -BLS technique. The waveguide spin-wave intensity pattern for odd numbers  $n$  is mapped in the lower panel of Fig. 1(c) (see Supplemental Material Movie 1 [50]). The results show that the interference of the odd modes results in a symmetric rhombohedral-shaped channel. Here, mathematically, the phase differences of the lower modes ( $n = 1, 3$ ) between the adjacent nodes [I, II, and III in Fig. 1(c)] of the spin-wave pattern are approximately  $2q\pi + \pi$ , where  $q$  is an arbitrary integer, as shown in Fig. 1(d).

Introducing new modes to interfere with the existing modes should modify this flow pattern. Accordingly, we consider the even modes because they have the same frequency as the previously considered odd modes and therefore the coherent interference would lead to a time-invariant pattern and because they should be easy to excite and should have similar lifetimes to the odd modes in the waveguides. In contrast to the odd modes, the even modes have antisymmetric patterns; in other words,  $m_n(x, y) + m_n(x, w-y) = 0$  for even  $n$  according to Eq. (3). The patterns of the first two even modes are mapped in Fig. 2(a).

The interference patterns are strongly depended on the difference of the initial phases ( $\Delta\varphi = \varphi_{\text{odd}} - \varphi_{\text{even}}$ ), meaning that the waveguide spin-wave channels can be controlled through tuning  $\Delta\varphi$  between the odd and the even modes. For our

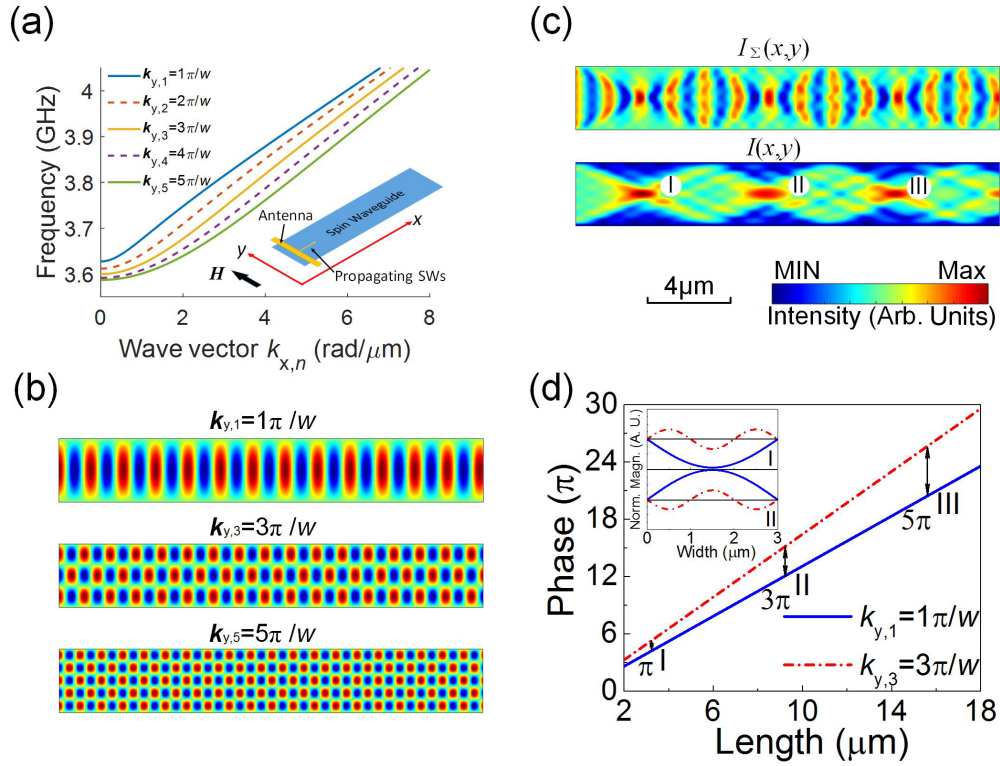


FIG. 1. Theoretical calculated results: (a) Dispersion curves for the first five Damon-Eshbach mode waveguide spin waves propagating in a YIG microstrip. The inset depicts a schematic of the studied model. (b) The spatial distribution of  $m_n(x, y)$  for the first three odd modes at the initial phase ( $-2\pi ft + \varphi_n = 0$ ). (c) Interference patterns of the first few odd modes ( $n \leq 11$ ), upper panel:  $I_\Sigma(x, y)$  and lower panel:  $I(x, y)$ . (d) The phase shift of the first and third modes along the length. Inset shows the normalized dynamic magnetization distribution across the stripe at the first and second nodes, as indicated in panel (c).

analysis, some representative values ( $0, \pi/2, \pi$ , and  $3\pi/2$ ) for  $\Delta\varphi$  were chosen by fixing  $\varphi_{\text{odd}} = 0$  in Eq. (3), and using

$\varphi_{\text{even}} = 0, \pi/2, \pi$ , and  $3\pi/2$ , respectively. The corresponding patterns of  $I_\Sigma(x, y)$  and  $I(x, y)$  are shown in Figs. 2(b)–2(e)

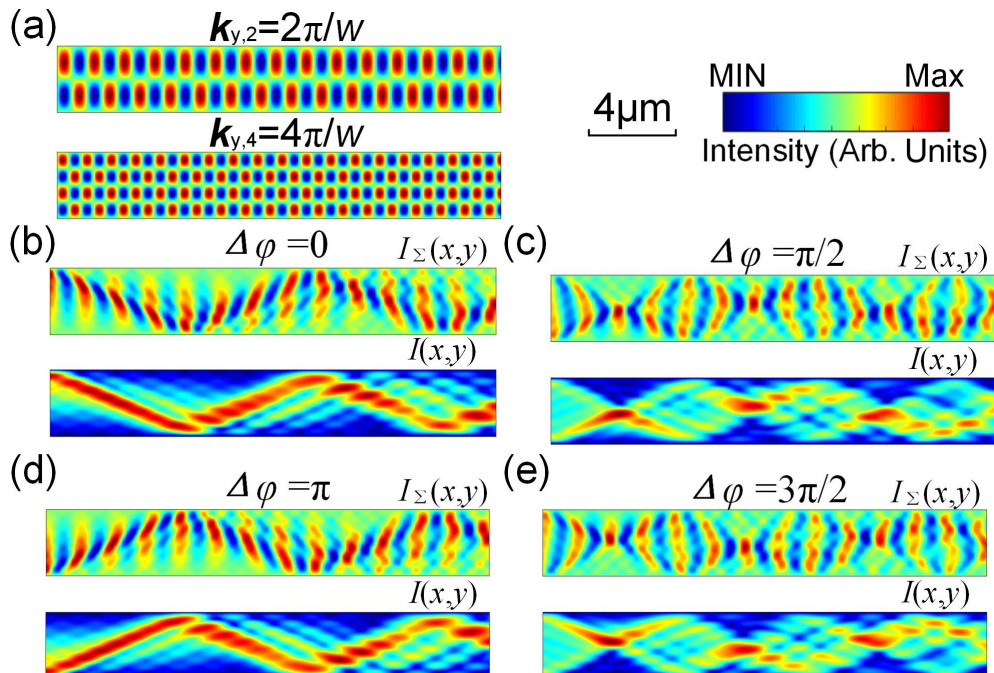


FIG. 2. (a) The spatial distribution of  $m_n(x, y)$  for the first two even modes at the initial phase ( $-2\pi ft + \varphi_n = 0$ ). Interference patterns of the odd and even modes with a phase difference (b)  $\Delta\varphi = 0$ , (c)  $\pi/2$ , (d)  $\pi$ , and (e)  $3\pi/2$ , upper panel:  $I_\Sigma(x, y)$  and lower panel:  $I(x, y)$ .

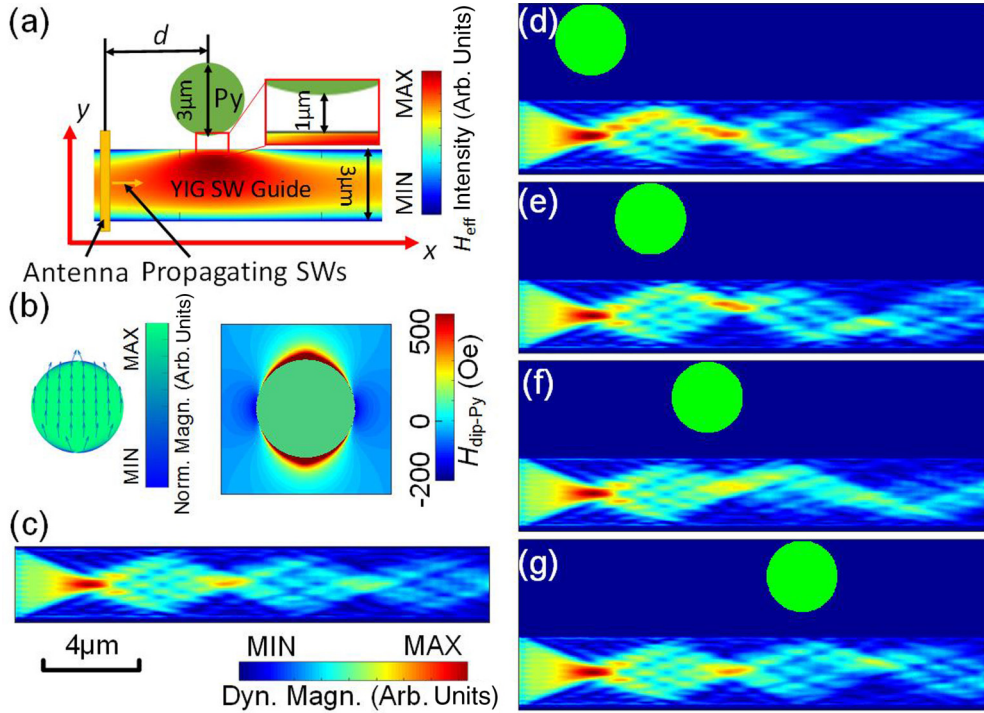


FIG. 3. (a) Schematic of the simulated model. The colormap encodes the  $y$  component of the effective magnetic field ( $H_{\text{eff}}$ ) distribution inside of the YIG stripe with a permalloy (Py) dot (green, same hereinafter). (b) The  $y$  component of the normalized magnetization of the Py dot (left) and the static dipolar field (right) induced by the Py dot under 640 Oe external field applied along the  $y$  direction. The colormaps encode the magnetization inside the Py dot and the field distribution outside the Py dot. The blue arrows in the left panel indicate the directions of the magnetization. Patterns of the waveguide spin waves propagating in the (c) single YIG stripe, and the YIG stripe with a lateral permalloy dot at the (d) first node, (e) first antinode, (f) second node, and (g) second antinode.

(see Supplemental Material Movies 2–5 [50]). Compared with Fig. 1(c), the introduction of the new modes changes the patterns from symmetric diamondlike shapes to antisymmetric zigzag shapes. In addition, the paths of the waveguide spin waves can be continuously changed if  $\Delta\varphi$  is varied continuously in the range from 0 to  $2\pi$ . Because the phase shift is given by  $\Delta\varphi = kd$ , we investigated the control of the  $\Delta\varphi$  via two different pathways: the change of distance  $d$ , and the wave vector  $k$ . The spin-wave patterns in this work were similar to those reported earlier [41,42]. In these papers the self-focusing and the antisymmetric “snakelike structures” patterns of magnetostatic backward volume waves were observed in thick YIG films due to the interplay between the diffraction of the beam and nonlinearity caused by the high microwave power of the input antenna.

### III. MICROMAGNETIC MODELING

In the discussions above, the introduction of even modes allows the manipulation of the propagating waveguide spin waves through their interference with the intrinsic odd modes. The generation of even modes can be realized via the breaking the translational symmetry, such as by passing through curved waveguides [46,51]. In this work, we demonstrate that the magnetic symmetry of the single YIG microstripe can be broken by a non-symmetric distribution of lateral micromagnets, i.e., a permalloy dot, as shown in Fig. 3(a). The simulations were performed using MuMax3 [52]. The material

parameters for permalloy (Py) were  $M_s(\text{Py}) = 1.08 \times 10^4$  G,  $A(\text{Py}) = 1.3 \times 10^{-11}$  J/m and  $\alpha(\text{Py}) = 0.01$  [53]. The external magnetic field ( $H_{\text{ext}}$ ) set in the simulation was 640 Oe. The  $y$  component of the static  $H_{\text{eff}}$  distribution inside the YIG microstripe is shown in the color map of Fig. 3(a). The  $y$  components of the normalized magnetization of the Py dot and the induced static dipolar field by Py dot ( $H_{\text{dip-Py}}$ ) are shown in the color maps of Fig. 3(b). Because of the strong induced dipolar field, the lateral symmetry of  $H_{\text{eff}}$  across the width of the waveguide was gradually broken in the segment close to the permalloy dot, while  $H_{\text{eff}}$  was symmetric in the segments far away from the permalloy dot. To excite the spin waves, we applied a continuous excitation of the sine function  $h_x = h_0 \sin(2\pi ft)$  in the antenna region with  $f = 4$  GHz and  $h_0 = 1$  Oe, which is small enough to avoid nonlinear effects. The total simulation time was 80 ns, to ensure that the system reaches a steady state. Figure 3(c) shows the pattern of the waveguide spin waves in a single YIG microstripe, which is similar to the theoretical result in Fig. 1(c). The results show that the length of the spin-wave modulation period in the simulation is slightly different from the one previously calculated analytically, which is because of the reduced effective width by the demagnetizing field and the slightly different  $H_{\text{ext}}$ .

Figures 3(d)–3(g) show the propagating waveguide spin-wave patterns when the permalloy dot was located at the first node, first antinode, second node, and second antinode (see Supplemental Material Movies 6–10 [50]). These patterns are qualitatively in accordance with the patterns of  $\Delta\varphi = \pi$ ,

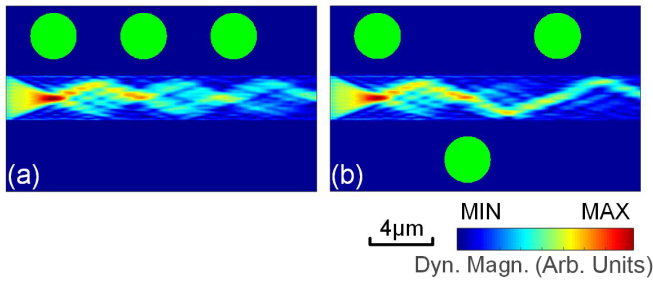


FIG. 4. Simulated patterns of the waveguide spin waves propagating in YIG stripe with three lateral permalloy dots at the first three nodes (a) on one side and (b) with the second permalloy dot on the opposite side.

$3\pi/2$ ,  $0$ , and  $\pi/2$  in Fig. 2. Practically, the odd modes are excited in the antenna region, with  $\varphi_{\text{odd}} = 0$ . As the odd modes propagate along the stripe for a certain distance  $d$ , the phases shift by  $kd$ , where  $k$  is the corresponding wavevectors. At the first node position, the phase shift of the main contributing odd modes is approximately  $\varphi_{\text{odd}} = 2q\pi + \pi$  as discussed above. Here, because the symmetry is broken, the even modes are excited with  $\varphi_{\text{even}} = 0$ , and therefore the final interference pattern in Fig. 3(d) agrees well with the analytical result of  $\Delta\varphi = \pi$ . Similarly, the patterns of Figs. 3(e)–3(g) agree with  $\Delta\varphi = 3\pi/2$ ,  $0$ , and  $\pi/2$ , respectively.

In addition, the initial phase of the newly introduced even modes is also determined by the side the permalloy dot is located on. For example, comparing Figs. 3(d) and 3(f), the patterns of the waveguide spin waves after passing by the permalloy dot are inversely mirrored. A similar behavior is also observed in Figs. 3(e) and 3(g). These results indicate that a phase difference of  $\pi$  can be induced by placing the permalloy dot on the other side. Therefore, the even modes can be annihilated (enhanced) by the destructive (constructive) interference with other even modes generated by other micromagnets in close proximity to the waveguide on the same (other) side one period away. To demonstrate this relationship, we simulated the waveguide spin-wave patterns in a YIG microstripe with three permalloy dots distributed on one side and two sides, as shown in Figs. 4(a) and 4(b), respectively (see Supplemental Material Movies 11 and 12 [50]). In Fig. 4 (a), the permalloy dots were located at the first three nodes on one side. The waveguide spin waves experienced the following processes: (1) The first even mode (EM1) was generated with  $\varphi_{\text{EM1}} = 0$  at the first node, resulting in the waveguide spin waves propagating nonsymmetrically in the following self-focusing period; (2) the second even mode (EM2) was generated with  $\varphi_{\text{EM2}} = 0$  at the second node. However, at this point, the first even mode has a phase shift of  $\pi$  and destructively interferes with the second even mode. Therefore, the asymmetry disappeared in the next period; (3) the third even mode (EM3) was generated with  $\varphi_{\text{EM3}} = 0$  at the third node again, leading to the following asymmetrical pattern. In contrast, in Fig. 4(b), the second even mode was generated with  $\varphi_{\text{EM2}} = \pi$  and thus constructively interfered with the first even mode, as did the third even mode. The antisymmetric component was therefore increased compared with Fig. 3(c).

In this section, we demonstrated that  $\Delta\varphi$  can be tuned by changing the relative position of permalloy dots near the YIG microstripe, including the distance  $d$  to the excitation and the side on which it is located. Changing the distance  $d$  leads to a phase shift of odd modes with  $kd$ , and switching the sides causes even modes phases to shift by  $\pi$ . Using multiple permalloy dots introduces multiple even modes, whose constructive (destructive) interference increases (decreases) the antisymmetric component of the propagating waveguide spin waves.

#### IV. EXPERIMENTS

According to the dispersion relation described by Eq. (1), the wave vectors  $k$  of the waveguide spin waves with specific frequencies can be modified by  $H_0$ , which is the most common tunable parameter among the variables in the equation if the devices are already fabricated [54,55]. We have also performed experimental studies of the structures similar to those described in the Analytical and Micromagnetic Sections. Figure 5(a) shows a schematic illustration of the test sample consisting of an input antenna, patterned YIG stripe and permalloy dot. Py and YIG (both are 75-nm-thin) samples were grown using magnetron sputtering in Ar atmosphere and stoichiometric targets. YIG films were then *ex situ* annealed in air to improve their crystallinity and magnetic properties. The typical linewidth  $\Delta H$  of the annealed YIG film at a frequency of 4 GHz used in our experiments was  $\sim 2.7$  Oe. As-fabricated thin films have the magnetization of saturation ( $M_s$ ) values of 9760 G and 1960 G, and damping factors ( $\alpha$ ) of  $7.3 \times 10^{-3}$  and  $2.1 \times 10^{-4}$  for Py, and YIG films, accordingly. The input antenna, 4.5- $\mu\text{m}$ -wide YIG stripes, and Py dot (4.5  $\mu\text{m}$  in diameter) were defined using multistep electron-beam lithography and the lift-off technique (see Appendices A and B for details). For the excitation of the spin waves, the shortened end of a coplanar waveguide made of Ti(20 nm)/Au(500 nm) with a width approximately 2  $\mu\text{m}$  was placed on top of the end of the YIG microstripe. The spin waves excited by the antenna structure connected with a microwave generator can reach a frequency of in several tens of gigahertz. In this work, we fixed the frequency at 4 GHz and output microwave power at 10 dBm.

All the observations of the spin waves were performed using microfocused Brillouin light scattering ( $\mu$ -BLS) [56] with a laser wavelength of 532 nm. First, we measured the 4 GHz spin-wave intensity versus  $H_{\text{ext}}$  in a single YIG stripe with the laser spot fixed at the center of the cross in the red circle as indicated in Fig. 5(a). The BLS intensities versus magnetic field is shown in Fig. 5(b), where the peak is located around 650 Oe. Consequently, the 4-GHz spin waves propagate with the highest efficiency in the YIG microstripe for  $H_{\text{ext}} \approx 650$  Oe. Subsequently, the intensity patterns of propagating spin waves in a single YIG microstripe under 630 and 670 Oe were mapped as shown in Figs. 5(c) and 5(d). By comparing the two patterns in a single YIG microstripe the self-focus period was expanded with increased of  $H_{\text{ext}}$  because of the collective decrease and convergence of the  $ks$  for odd modes [57,58].

Next, we studied the sample with the 4.5- $\mu\text{m}$  permalloy dot deposited on one side of the YIG microstripe  $\sim 3.5 \mu\text{m}$

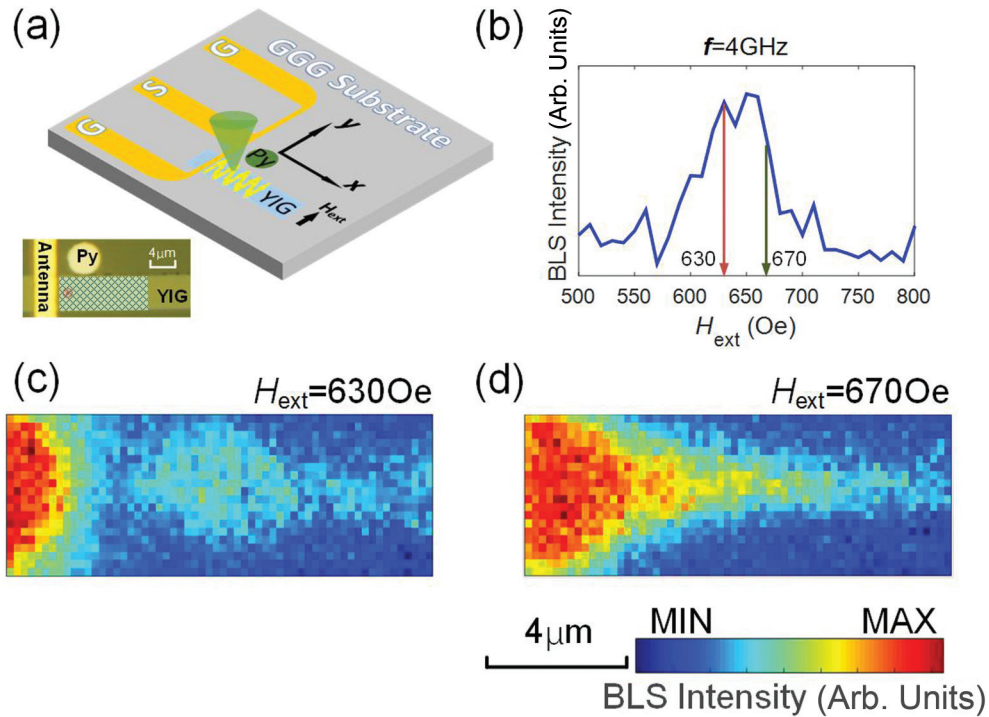


FIG. 5. (a) Schematic illustration of the device layout. The inset shows an optical microscopy image of the device. The spin-wave patterns were imaged in the grid region. (b) 4-GHz spin-wave BLS intensity in a single YIG stripe vs.  $H_{\text{ext}}$  measured with the laser spot fixed at the center of the cross in the red circle. (c, d) BLS intensity images at two different applied fields.

away from the antenna almost at the first node of the pattern measured for 630 Oe. The spin-wave intensities were imaged in the same region of the YIG microstripe under various magnetic field conditions (610 to 690 Oe), as shown in Fig. 6.

The BLS patterns in the YIG stripe without/permalloy dot under 630 Oe [Figs. 5(c) and 6(b)] are in accordance with Figs. 3(c) and 3(d), where the spin waves flow toward the permalloy dot. In contrast, by comparing the patterns of Figs. 6(b) and 6(d), the effect of the permalloy dot at 670 Oe is to squeeze the spin-wave flow toward the other side instead of attracting to the same edge, indicating that the generated even modes here have a  $\pi$  phase difference with those in Fig. 6(b). According to Fig. 5(b), the 4-GHz spin waves propagate with the largest amplitude in the middle of the YIG microstripe under  $H_{\text{ext}} \approx 650$  Oe. The spin waves with a specific frequency in the waveguide could reach its highest intensity near the ferromagnetic resonant field, and similar phenomena were observed in measurements of the spin waves localized at the two edges of a stripe. The two SWs beams were split more with the increase of the field at a fixed frequency [59], and the decrease of the frequency at a fixed field [35] because of the demagnetizing magnetic field. To demonstrate this effect, the  $H_{\text{eff}}$  across the YIG stripe versus its width is plotted in Fig. 7(a) where the black dash line indicates the level of 650 Oe. The integrated BLS normalized intensities across the width close to permalloy dot were measured for different magnetic fields, as shown in Fig. 7(b). The intersections between the dashed line and solid lines in Fig. 7(a) agree with the locations of the BLS intensity peaks in Fig. 7(b) for the different magnetic fields. The presence of the permalloy dot introduces an additional static dipolar field that shifts the position of the effective field

to be 650 Oe closer to (further away from) the permalloy dot when  $H_{\text{ext}} < 650$  Oe ( $H_{\text{ext}} > 650$  Oe), attracting (repelling) the spin-wave flow.

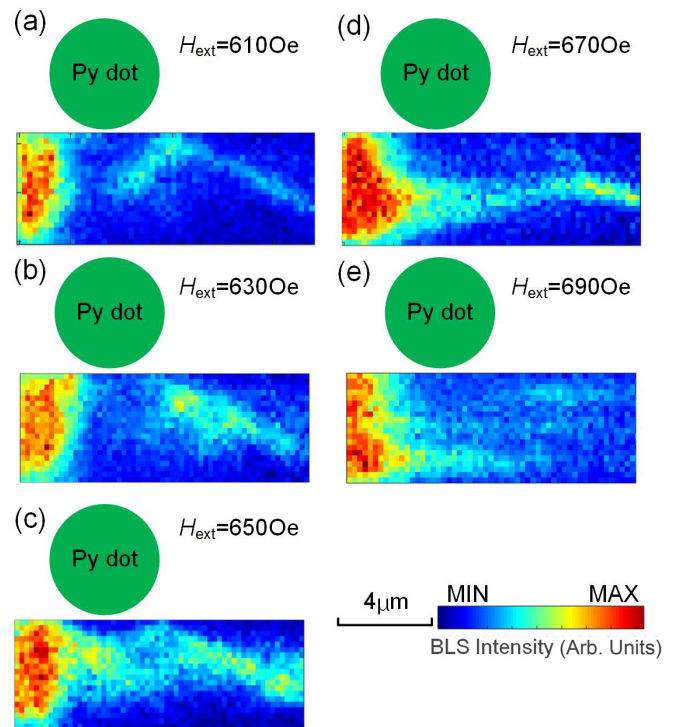


FIG. 6. 4-GHz spin-wave intensity patterns in YIG microstripe with a lateral permalloy dot measured at the externally applied magnetic fields of (a) 610, (b) 630, (c) 650, (d) 670, and (e) 690 Oe.

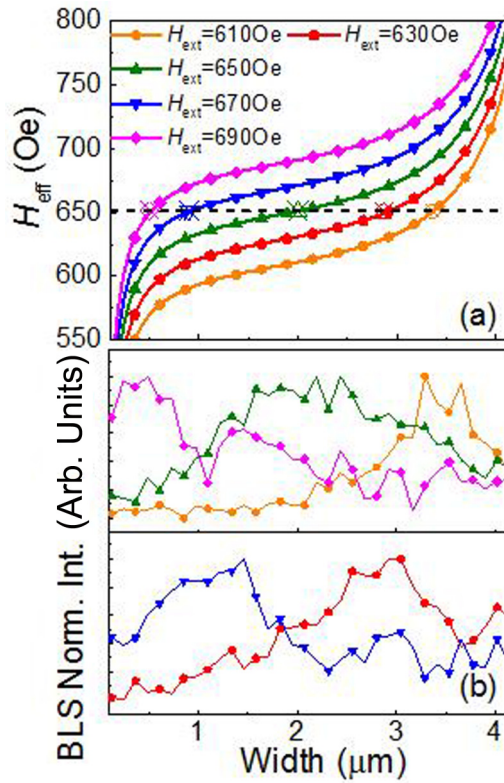


FIG. 7. (a) Simulated  $H_{\text{eff}}$  and (b) integrated BLS normalized intensities across the YIG microstripe with a permalloy dot near at different  $H_{\text{ext}}$  varied from 610 to 690 Oe. The horizontal black dash line in (a) indicates the field of 650 Oe. The intersections between the black dash line and the solid lines agree with the BLS intensity peaks. Panels (a) and (b) share the same legend.

## V. CONCLUSION

In summary, we demonstrated a new method, using the interference of different spin waves, to manipulate the channels of the waveguide spin waves propagating in a magnetic microstripe. The waveguide spin-wave channels can be tuned by the phase difference  $\Delta\varphi$  between the intrinsic odd modes, which are preferred by homogenous excitation. Additional even modes can be introduced via breaking the magnetic symmetry through the non-symmetrical placement of a

permalloy dot next to the wave guide. The phase shift  $\Delta\varphi$  is controlled by the relative position of the permalloy dot to the antenna and the external magnetic field  $H_{\text{ext}}$ . An additional phase difference of  $\pi$  can be introduced if the permalloy dot is located on the opposite side of the microstripe or the  $H_{\text{ext}}$  exceeds the field for the most efficient spin-wave propagation. These findings can assist with magnonic engineering, for example such as in designing a multiplexer combined with the piezoelectric strain control of the micromagnets or the reconfigurable phase shifters, which are of interest for spin-wave interference-based logic gate device concepts. Furthermore, with the suitable design of additional magnetic structures with sufficiently high anisotropy, the additional stray field may be modulated in a bistable manner, which could provide additional possibilities for the energy-efficient and non-volatile control of spin-wave propagation. Last, the described structures can also serve as a model system for fundamental studies of the physics of geometrically confined spin waves.

## ACKNOWLEDGMENTS

All work was performed at the Argonne National Laboratory and supported by the Department of Energy, Office of Science, Materials Science and Engineering Division. The use of the Centre for Nanoscale Materials was supported by the US Department of Energy (DOE), Office of Sciences, Basic Energy Sciences (BES), under Contract No. DE-AC02-06CH11357. Z.Z. acknowledges additional financial support from the China Scholarship Council (Grant No. 201706160146) for a research stay at Argonne. J.H. acknowledges financial support from the Conselho Nacional de Desenvolvimento Científico e Tecnológico (CNPq)-Brasil. W.Z. acknowledges support from US National Science Foundation under Grant No. DMR-1808892. The authors thank Prof. Andrii V. Chumak for constructive discussions.

## APPENDIX A: SAMPLE FABRICATION

Microstructured YIG stripe and the lateral Py dot were deposited on commercial polished (111)-oriented gadolinium gallium garnet ( $\text{Gd}_3\text{Ga}_5\text{O}_{12}$ , GGG). YIG was RF magnetron sputtered at room temperature (RT) from a stoichiometric YIG target. The Ar gas flow, chamber pressure, and sputtering

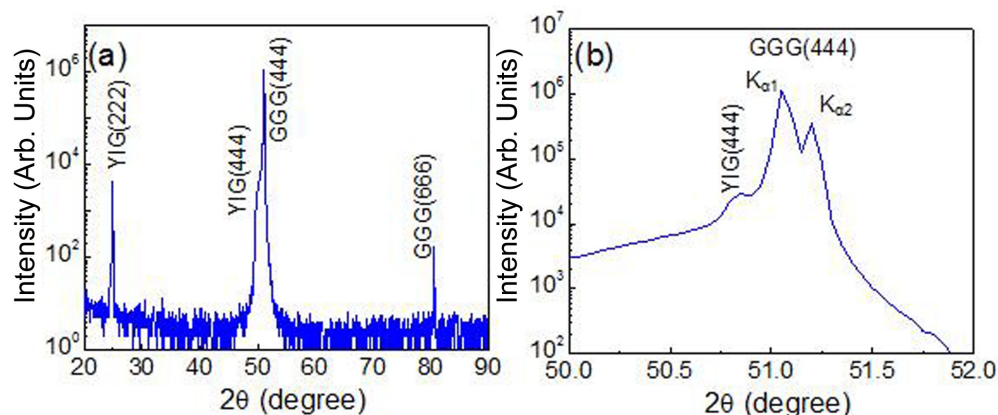


FIG. 8. (a) XRD data of a 75-nm annealed YIG film and (b) the zoomed-in data in (a) showing the YIG (444) peak.

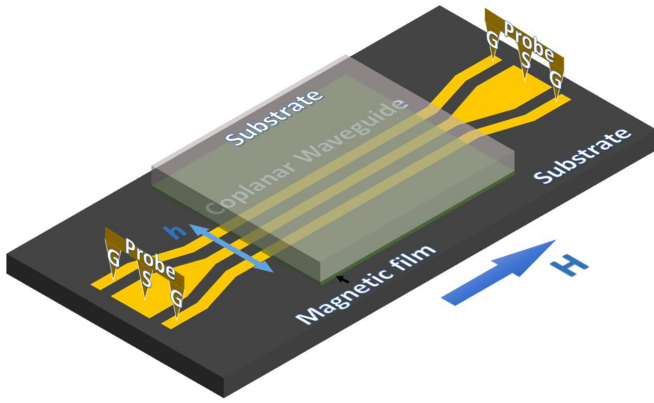


FIG. 9. Schematic diagram of the VNA-FMR. The continuous magnetic films were placed on the coplanar waveguide structure. The applied external magnetic static field  $H$  was perpendicular to the microwave field  $h$ .

power were maintained at 16 sccm, 10 mTorr, and 75 W, respectively. The microstructures were defined using electron-beam lithography (Raith 150) on PMGI SF6/ZED520 bilayer resists, creating an undercut cross-section profile. Because GGG is an insulator, a 5-nm Au layer was DC sputtered on the resists to avoid charge effects during electron-beam exposure. Before the development, the Au was removed by exposure in a gold etcher. Then, the electron beam exposed resists were developed in ZEDN50 (for ZED520) and 101A

(for PMGI SF6) developers, respectively. After the deposition of YIG, the resist was removed by Shipley 1165 with only the microstripe structures left. The YIG was subsequently annealed *ex situ* at 850 °C for 3 h in a tube furnace, with ramped-up time of 6 h and ramped-down time of 14 h. After the YIG microstripe fabrication, the coplanar waveguide with a shorted end made of Ti(20 nm)/Au(500 nm) was fabricated via optical lithography. After the  $\mu$ -BLS measurement on the single YIG stripe, the Py dot was DC magnetron sputtered laterally near the YIG stripe, followed by the same electron-beam lithography process. The precise alignment was performed in this step. The corresponding continuous YIG film and Py film capped with SiO<sub>2</sub> (15 nm) on the whole substrates were also fabricated using the same process and fabrication parameters to characterize the material features.

## APPENDIX B: MATERIALS CHARACTERIZATION

YIG films crystalline structure was confirmed by x-ray diffraction (XRD). The XRD patterns are shown in Figs. 8(a) and 8(b). The data confirm the YIG phase is (111)-oriented without the existence of any additional phases.

The flip-chip vector network analyzer ferromagnetic resonance (VNA-FMR) method (Fig. 9) was applied to the continuous films extended on the whole substrates to characterize the magnetic properties. We measured the transmission coefficient by sweeping the frequency at every fixed field. Therefore, the frequency swept linewidths ( $\Delta f_{\text{VNA}}$ ) were obtained via Lorentz fitting. Detailed steps, including the conversion

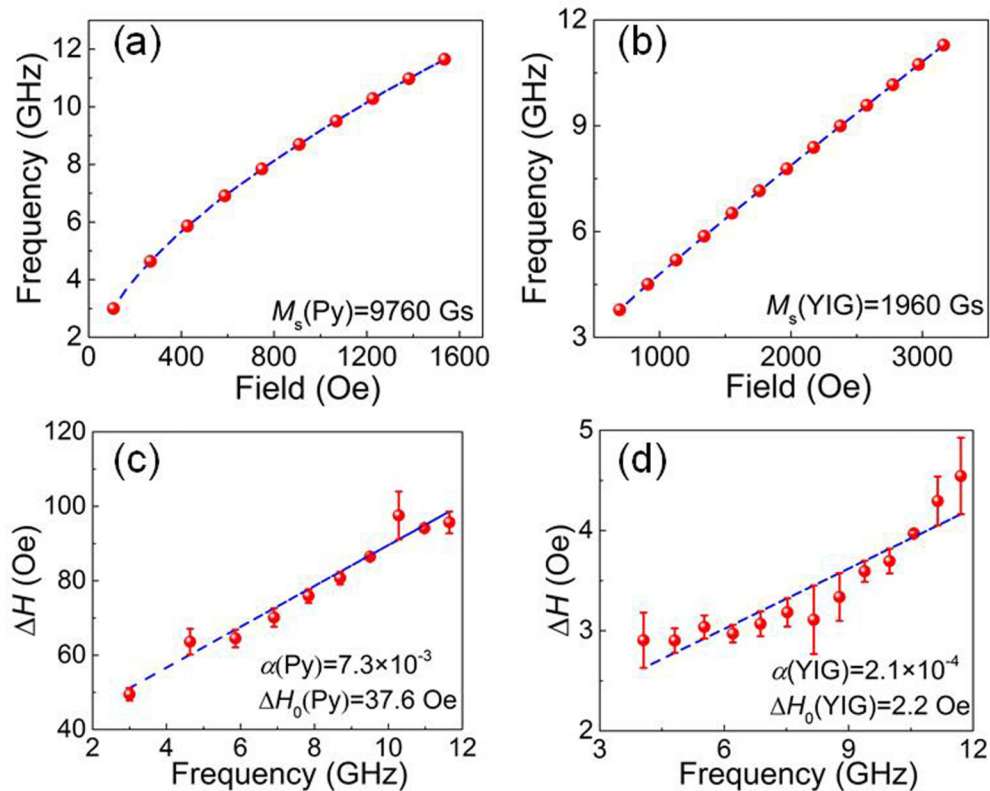


FIG. 10. (a) Py and (b) YIG FMR frequency as a function of the magnetic field. Error bars are smaller than the symbol size. (c) Py and (d) YIG FMR linewidth  $\Delta H$  as a function of the resonance frequency

from  $\Delta f_{\text{VNA}}$  to  $\Delta H$ , are based on those presented in Ref. [60]. The resonance frequencies as a function of the magnetic field were fitted according to Kittel's equation:

$$f_{\text{res}} = \gamma \sqrt{H(H + M_s)}, \quad (\text{B1})$$

where the  $M_s$  was yielded. In addition,  $\alpha$  can be obtained through the following fit:

$$\Delta H = \frac{2\alpha f_{\text{res}}}{\gamma} + \Delta H_0, \quad (\text{B2})$$

where  $\Delta H_0$  denotes the inhomogeneous linewidth broadening. Figure 10 depicts the magnetic properties of the magnetic films in the experiment.

- 
- [1] A. V. Chumak, V. I. Vasyuchka, A. A. Serga, and B. Hillebrands, *Nat. Phys.* **11**, 453 (2015).
- [2] M. Krawczyk and D. Grundler, *J. Phys.: Condens. Matter* **26**, 123202 (2014).
- [3] A. Haldar, D. Kumar, and A. O. Adeyeye, *Nat. Nano* **11**, 437 (2016).
- [4] Q. Wang, P. Pirro, R. Verba, A. Slavin, B. Hillebrands, and A. V. Chumak, *Sci. Adv.* **4**, e1701517 (2018).
- [5] B. Lenk, H. Ulrichs, F. Garbs, and M. Münzenberg, *Phys. Rep.* **507**, 107 (2011).
- [6] Y. Li, T. Polakovic, Y.-L. Wang, J. Xu, S. Lendinez, Z. Zhang, J. Ding, T. Khaire, H. Saglam, R. Divan, J. Pearson, W.-K. Kwok, Z. Xiao, V. Novosad, A. Hoffmann, and W. Zhang, [arXiv:1902.09715](https://arxiv.org/abs/1902.09715) [Phys. Rev. Lett. (to be published)].
- [7] J. Holanda, D. S. Maior, A. Azevedo, and S. M. Rezende, *Nat. Phys.* **14**, 500 (2018).
- [8] S. Mansfeld, J. Topp, K. Martens, J. N. Toedt, W. Hansen, D. Heitmann, and S. Mendach, *Phys. Rev. Lett.* **108**, 047204 (2012).
- [9] N. Loayza, M. B. Jungfleisch, A. Hoffmann, M. Bailleul, and V. Vlaminck, *Phys. Rev. B* **98**, 144430 (2018).
- [10] J. Stigloher, M. Decker, H. S. Körner, K. Tanabe, T. Moriyama, T. Taniguchi, H. Hata, M. Madami, G. Gubbiotti, K. Kobayashi, T. Ono, and C. H. Back, *Phys. Rev. Lett.* **117**, 037204 (2016).
- [11] S.-K. Kim, S. Choi, K.-S. Lee, D.-S. Han, D.-E. Jung, and Y.-S. Choi, *Appl. Phys. Lett.* **92**, 212501 (2008).
- [12] R. G. Kryshnal and A. V. Medved, *J. Magn. Magn. Mater.* **426**, 666 (2017).
- [13] S. S. Mukherjee, J. H. Kwon, M. Jamali, M. Hayashi, and H. Yang, *Phys. Rev. B* **85**, 224408 (2012).
- [14] P. Pirro, T. Brächer, K. Vogt, B. Obry, H. Schultheiss, B. Leven, and B. Hillebrands, *Phys. Status Solidi (b)* **248**, 2404 (2011).
- [15] A. V. Chumak, P. Dhagat, A. Jander, A. A. Serga, and B. Hillebrands, *Phys. Rev. B* **81**, 140404 (2010).
- [16] V. Vlaminck and M. Bailleul, *Science* **322**, 410 (2008).
- [17] R. E. Camley, *Phys. Rev. B* **89**, 214402 (2014).
- [18] H. Kurebayashi, O. Dzyapko, V. E. Demidov, D. Fang, A. J. Ferguson, and S. O. Demokritov, *Nat. Mater.* **10**, 660 (2011).
- [19] C. L. Ordóñez-Romero, B. A. Kalinikos, P. Krivosik, W. Tong, P. Kabos, and C. E. Patton, *Phys. Rev. B* **79**, 144428 (2009).
- [20] X. Zhang, C.-L. Zou, L. Jiang, and H. X. Tang, *Phys. Rev. Lett.* **113**, 156401 (2014).
- [21] T. Schneider, A. A. Serga, B. Leven, B. Hillebrands, R. L. Stamps, and M. P. Kostylev, *Appl. Phys. Lett.* **92**, 022505 (2008).
- [22] A. A. Nikitin, A. B. Ustinov, A. A. Semenov, A. V. Chumak, A. A. Serga, V. I. Vasyuchka, E. Lähderanta, B. A. Kalinikos, and B. Hillebrands, *Appl. Phys. Lett.* **106**, 102405 (2015).
- [23] T. Fischer, M. Kewenig, D. A. Bozhko, A. A. Serga, I. I. Syvorotka, F. Ciubotaru, C. Adelman, B. Hillebrands, and A. V. Chumak, *Appl. Phys. Lett.* **110**, 152401 (2017).
- [24] S. Klingler, P. Pirro, T. Brächer, B. Leven, B. Hillebrands, and A. V. Chumak, *Appl. Phys. Lett.* **105**, 152410 (2014).
- [25] Y. Kajiwar, K. Harii, S. Takahashi, J. Ohe, K. Uchida, M. Mizuguchi, H. Umezawa, H. Kawai, K. Ando, and K. Takahashi, *Nature* **464**, 262 (2010).
- [26] A. Khitun and K. L. Wang, *J. Appl. Phys.* **110**, 034306 (2011).
- [27] K. Alexander, B. Mingqiang, and L. W. Kang, *J. Phys. D Appl. Phys.* **43**, 264005 (2010).
- [28] A. V. Chumak, V. I. Vasyuchka, A. A. Serga, M. P. Kostylev, V. S. Tiberkevich, and B. Hillebrands, *Phys. Rev. Lett.* **108**, 257207 (2012).
- [29] A. V. Chumak, A. A. Serga, and B. Hillebrands, *Nat. Commun.* **5**, 4700 (2014).
- [30] T. Sebastian, T. Brächer, P. Pirro, A. A. Serga, B. Hillebrands, T. Kubota, H. Naganuma, M. Oogane, and Y. Ando, *Phys. Rev. Lett.* **110**, 067201 (2013).
- [31] S. Li, W. Zhang, J. Ding, J. E. Pearson, V. Novosad, and A. Hoffmann, *Nanoscale* **8**, 388 (2016).
- [32] M. B. Jungfleisch, W. Zhang, W. Jiang, H. Chang, J. Sklenar, S. M. Wu, J. E. Pearson, A. Bhattacharya, J. B. Ketterson, M. Wu, and A. Hoffmann, *J. Appl. Phys.* **117**, 17D128 (2015).
- [33] V. E. Demidov, M. P. Kostylev, K. Rott, P. Krzyszczyk, G. Reiss, and S. O. Demokritov, *Appl. Phys. Lett.* **95**, 112509 (2009).
- [34] R. W. Damon and J. R. Eshbach, *J. Phys. Chem. Solids* **19**, 308 (1961).
- [35] V. E. Demidov, S. O. Demokritov, K. Rott, P. Krzyszczyk, and G. Reiss, *Appl. Phys. Lett.* **92**, 232503 (2008).
- [36] P. Pirro, T. Brächer, A. V. Chumak, B. Lägél, C. Dubs, O. Surzhenko, P. Görnert, B. Leven, and B. Hillebrands, *Appl. Phys. Lett.* **104**, 012402 (2014).
- [37] V. E. Demidov and S. O. Demokritov, *IEEE Trans. Magn.* **51**, 1 (2015).
- [38] C. Kittel, *Phys. Rev.* **110**, 1295 (1958).
- [39] V. E. Demidov, S. O. Demokritov, K. Rott, P. Krzyszczyk, and G. Reiss, *Phys. Rev. B* **77**, 064406 (2008).
- [40] V. E. Demidov, S. O. Demokritov, K. Rott, P. Krzyszczyk, and G. Reiss, *Appl. Phys. Lett.* **91**, 252504 (2007).
- [41] O. Buttner, M. Bauer, C. Mathieu, S. O. Demokritov, B. Hillebrands, P. A. Kolodin, M. P. Kostylev, S. Sure, H. Dotsch, V. Grimalsky, Y. Rapoport, and A. N. Slavin, *IEEE Trans. Magn.* **34**, 1381 (1998).
- [42] J. W. Boyle, S. A. Nikitov, A. D. Boardman, J. G. Booth, and K. Booth, *Phys. Rev. B* **53**, 12173 (1996).

- [43] V. V. Matyushev, A. A. Stashkevich, and A. I. Lukyanov, *J. Appl. Phys.* **74**, 3680 (1993).
- [44] K. Vogt, F. Y. Fradin, J. E. Pearson, T. Sebastian, S. D. Bader, B. Hillebrands, A. Hoffmann, and H. Schultheiss, *Nat. Commun.* **5**, 3727 (2014).
- [45] V. V. Matyushev, A. A. Stashkevich, and A. I. Lukyanov, *Optics Commun.* **92**, 31 (1992).
- [46] P. Clausen, K. Vogt, H. Schultheiss, S. Schäfer, B. Obry, G. Wolf, P. Pirro, B. Leven, and B. Hillebrands, *Appl. Phys. Lett.* **99**, 162505 (2011).
- [47] B. A. Kalinikos, *IEEE Proc. Microwaves Optics Antenn.* **127**, 4 (1980).
- [48] B. A. Kalinikos and A. N. Slavin, *J. Phys. C Solid State Phys.* **19**, 7013 (1986).
- [49] G. S. Abo, Y. Hong, J. Park, J. Lee, W. Lee, and B. Choi, *IEEE Trans. Magn.* **49**, 4937 (2013).
- [50] See Supplemental Material at <http://link.aps.org/supplemental/10.1103/PhysRevB.100.014429> for 12 movie files and 1 file for more detailed descriptions.
- [51] A. V. Sadovnikov, C. S. Davies, V. V. Kruglyak, D. V. Romanenko, S. V. Grishin, E. N. Beginin, Y. P. Sharaevskii, and S. A. Nikitov, *Phys. Rev B* **96**, 060401 (2017).
- [52] A. Vansteenkiste, J. Leliaert, M. Dvornik, M. Helsen, F. Garcia-Sanchez, and B. Van Waeyenberge, *AIP Adv.* **4**, 107133 (2014).
- [53] K.-S. Lee, D.-S. Han, and S.-K. Kim, *Phys. Rev. Lett.* **102**, 127202 (2009).
- [54] K. Vogt, H. Schultheiss, S. J. Hermsdoerfer, P. Pirro, A. A. Serga, and B. Hillebrands, *Appl. Phys. Lett.* **95**, 182508 (2009).
- [55] V. E. Demidov, S. Urazhdin, and S. O. Demokritov, *Appl. Phys. Lett.* **95**, 262509 (2009).
- [56] T. Sebastian, K. Schultheiss, B. Obry, B. Hillebrands, and H. Schultheiss, *Front. Phys.* **3**, 35 (2015).
- [57] T. Brächer, P. Pirro, B. Obry, B. Leven, A. A. Serga, and B. Hillebrands, *Appl. Phys. Lett.* **99**, 162501 (2011).
- [58] M. Kostylev, J.-G. Hu, and R. L. Stamps, *Appl. Phys. Lett.* **90**, 012507 (2007).
- [59] A. Talalaevskij, M. Decker, J. Stigloher, A. Mitra, H. S. Körner, O. Cespedes, C. H. Back, and B. J. Hickey, *Phys. Rev. B* **95**, 064409 (2017).
- [60] S. S. Kalarickal, P. Krivosik, M. Wu, C. E. Patton, M. L. Schneider, P. Kabos, T. J. Silva, and J. P. Nibarger, *J. Appl. Phys.* **99**, 093909 (2006).